Sea Surface Current Retrieval From Sequential SAR and Ocean Color Images for Eddy Kinematics Analysis: A Case Study in the Northern Tyrrhenian Sea

Xue Yang, Jinsong Chong, *Senior Member, IEEE*, and Yawei Zhao

***Abstract*—Sea surface currents (SSCs) are of great importance in monitoring the evolving dynamics of oceans and can be effectively obtained from sequential remote sensing images. However, the absence of traceable feature patterns in sequential remote sensing images constrains the capabilities for retrieving SSCs. In this article, an approach was presented to retrieve SSCs by merging currents derived from synthetic aperture radar (SAR) and ocean color (OC) images computed using the maximum cross-correlation (MCC) method. For different OC product performances in retrieving the surface currents, an evaluation criterion was used to select the optimal OC-derived currents before merging. The complete current field was obtained by merging SAR and optimal OC-derived currents based on the correlation coefficient weighted model. Statistical comparisons were performed between the merged and geostrophic currents obtained from the altimetry over the northern Tyrrhenian Sea. The two current fields were in good agreement, with a complex correlation coefficient of 0.65 in magnitude and 2.23° in phase. The oceanic eddy kinematic parameters were successfully calculated based on the complete current field obtained and used to analyze spatio-temporal evolution characteristics.**

***Index Terms*—Ocean color (OC), oceanic eddies, sea surface currents (SSCs), synthetic aperture radar (SAR).**

I. Introduction

SEA surface currents (SSCs) are a substantial part of global ocean circulation. SSCs can transport heat, mass, surfactants, ice floes, suspended matter, and biogeochemical properties, crucially influencing global heat and flux exchange [1], [2]. Eddies are widespread in oceans and are more energetic than the surrounding currents [3]. SSCs play an important role in eddy kinematics analysis [4], which is challenging to retrieve on a large scale using traditional measurement devices such as buoys and acoustic Doppler current profilers.

Satellite remote sensing techniques provide large spatial coverage and regular observations of the ocean surface [5].

Satellite altimetry was specifically designed to measure global surface geostrophic currents [6]. Novel methodologies are available for deriving SSCs over regional seas and coastal zones using optical remote sensing and synthetic aperture radar (SAR) images. The maximum cross-correlation (MCC) method is a typical approach used for computing ocean currents using sequential satellite images [7]. It has been demonstrated to be effective in estimating currents from advanced very high-resolution radiometer thermal infrared images [8], [9], [10] and ocean color (OC) images [11], [12] by tracking the gradient of surface patterns induced by water mass advection. The weak gradient of surface patterns in satellite images cannot produce reliable vectors, therefore, the current fields derived from different optical satellite images are merged to increase the spatial coverage of the current fields [13], [14], [15], [16], [17]. However, most optical remote-sensing images encounter data loss caused by cloud cover. Studies have shown that approximately 70% of oceans are covered by clouds [19], therefore, cloud coverage is a problem that cannot be ignored in SSC estimation.

As an active remote-sensing instrument, SAR can provide observations of ocean surfaces under cloudy and nighttime conditions. Thus, SAR observations may complement optical remote sensing for estimating SSCs. Many studies have shown that SAR can be used for current estimation [20], [21], [22]. Lyzenga and Marmorino [23] estimated ocean surface currents by tracking ocean surface slicks from a pair of airborne SAR images at 20 min intervals. Qazi et al. [24] computed ocean surface currents by tracking slicks from a pair of Envisat and ERS-2 SAR images at 30 min intervals. To effectively estimate ocean currents over a general time interval, identifiable features such as ocean surface oil slicks must be present in sequential SAR images. Many researchers have utilized wavelet transforms to describe texture features such as oil spills, thereby achieving the detection and classification of texture features in SAR images [25], [26], [27]. Recently, deep learning approaches have been widely

Manuscript received 14 August 2023; revised 26 November 2023 and 19 April 2024; accepted 11 May 2024. Date of publication 17 May 2024; date of current version 30 May 2024. This work was supported by the National Natural Science Foundation of China under Grant 62231024. *(Corresponding author: Jinsong Chong.)*

Xue Yang and Jinsong Chong are with the National Key Laboratory of Microwave Imaging Technology, Aerospace Information Research Institute, Chinese Academy of Sciences, Beijing 100190, China, and also with the School of Electronic, Electrical, and Communication Engineering, University of Chinese Academy of Sciences, Beijing 100049, China (e-mail: yangxue19@mails.ucas.ac.cn; lily@mail.ie.ac.cn).

Yawei Zhao is with the National Key Laboratory of Microwave Imaging Technology, Aerospace Information Research Institute, Chinese Academy of Sciences, Beijing 100190, China (e-mail: zhaoyw@aircas.ac.cn).

Digital Object Identifier 10.1109/JSTARS.2024.3402243

applied to target detection and classification based on satellite images [28], [29], [30], [31], [32], showing great potential for SAR image oil spill detection. Various effective deep-learning networks have been developed. For example, Akbarizadeh et al. proposed deep learning networks, such as OSDES_Net [33] and GreyWolfLSM [34], which can accurately detect oil spills on the sea surface in SAR images, reduce the influence of noise and sea surface clutter on texture features, and thus obtain SSCs more accurately.

However, under the influence of low wind [35], upwelling [36], and floating macroalgae [37], SAR images exhibit large areas of low backscatter, which appear dark and lack the characteristic textural features of oil slicks. Although traditional methods and deep learning techniques can effectively extract dark areas, oil slicks cannot be obtained. Therefore, spatial gaps in the extraction of sea-surface flow fields arise from the absence of traceable texture features in the low backscatter regions of SAR images.

To overcome this problem, the present study combined SAR and OC images for the first time to extract SSC fields. Our findings indicate the potential of SSC fields for complementarity and provide a fresh perspective for obtaining a complete SSC field.

This rest of this article is organized as follows: Section II describes the study area and data. Section III presents the methodology used in the study. The main results are presented in Section IV. A discussion is presented in Sections V. Finally, Section VI concludes this article, respectively.

II. Study Area and Data

A. Study Area

The Mediterranean Sea lies between the Eurasian and African plates and extends from 30°N to 45°N and 6°W to 36°E. It is divided into two basins by the Sicily Channel and the Strait of Messina. The depths vary between 2500 and 3500 m in the western basin and between 3500 and 4000 m in the eastern basin. Strong regional offshore winds, such as Mistral in the north and Scirocco in the south, influence the western Mediterranean and lead to the onset of large algal blooms. Owing to its special climatic characteristics and geographical location, the evaporation of the Mediterranean Sea greatly exceeds the precipitation and river runoff, therefore, the Mediterranean Sea has a high salinity, which is central to water circulation within the basin [38]. The study area is located in the Tyrrhenian Sea of the western Mediterranean, extending from 39°N to 43°N and from 9°E to 12°E. In the Tyrrhenian Sea. The flow spreads along the coast of Italy, with mesoscale turbulence and wind-induced eddies in the center of the basin. In the northern Tyrrhenian Sea, the westward "Ligurian Current" develops, the structure and mesoscale variability of which vary significantly by season [39], [40].

B. Data

SAR images were acquired from Envisat and ERS-2 provided by the European Space Agency (ESA, https://earth.esa.int/). The SAR images are delivered at a pixel sampling of 12.5 m by 12.5 m, with a geometric resolution of approximately 30 m in ground range by 30 m in azimuth. In Fig. 1, the red strip represents the coverage of five Envisat SAR images, and the black strip represents the coverage of five ERS-2 SAR images. The first SAR images for each strip were acquired at 09:33 UTC and 10:01 UTC on March 21, 2005. Envisat and ERS-2 are in the same orbit, and ERS-2 follows Envisat with a time lag of 30 min. Detailed information about the sequential SAR images is given in Table I.

OC images were obtained using an Envisat Medium-Resolution Imaging Spectrometer (MERIS) [41] and an Aqua Moderate-Resolution Imaging Spectroradiometer (MODIS) with spatial resolutions of 1200 and 1000 m, respectively. The green and blue areas in Fig. 1 show the coverage of MERIS and Aqua MODIS, respectively. OC images were downloaded from the Ocean Color website (https://oceancolor.gsfc.nasa.gov/). MERIS and MODIS provide OC products derived from different spectral channels. Table I illustrates that the common products of MERIS and MODIS are Chl (the chlorophyll-a concentration), Kd490 (the diffuse attenuation coefficient at 490 nm), and Rrs443 (the remote sensing reflectance at 443 nm).

III. Methodology

The procedure for SSC retrieval from sequential SAR and OC images is illustrated in Fig. 2 and can be summarized in three steps.

Step 1: Compute currents from a pair of SAR images. The processing of SAR images corresponds to the green rectangles in Fig. 2. Preprocessing of SAR images included radiometric calibration, filtering, registration and mosaic. Then, SAR images were used to retrieve SSC through the MCC method.

Step 2: Compute currents from multiple OC products. The pre-processing of OC images included resampling and registration. Subsequently, multiple pairs of OC images were used to retrieve SSC through the MCC method, respectively. Optimal currents were then selected for merging from the different OC-derived currents. The processing of OC images corresponds to the red rectangles in Fig. 2.

Step 3: Merge the SAR and optimal OC-derived currents to obtain the complete current field. The processing for this step corresponds to the blue rectangles in Fig. 2.

The following provides a detailed introduction divided into three parts: the MCC method, metrics for evaluating OC-derived currents, and calculation of merged currents. Section III-C also includes the calculation of eddy kinematic parameters to analyze the evolution characteristics of eddies.

A. MCC Method

A block diagram of the MCC method is shown in Fig. 3. The MCC method was used to retrieve the currents by automatically tracking the features in a pair of registered images [7]. A point $P_0(x_T, y_T)$ was selected in the first image, and a region centered on P_0 was selected as the template window T. A larger region centered at the same position as P_0 in the second image was

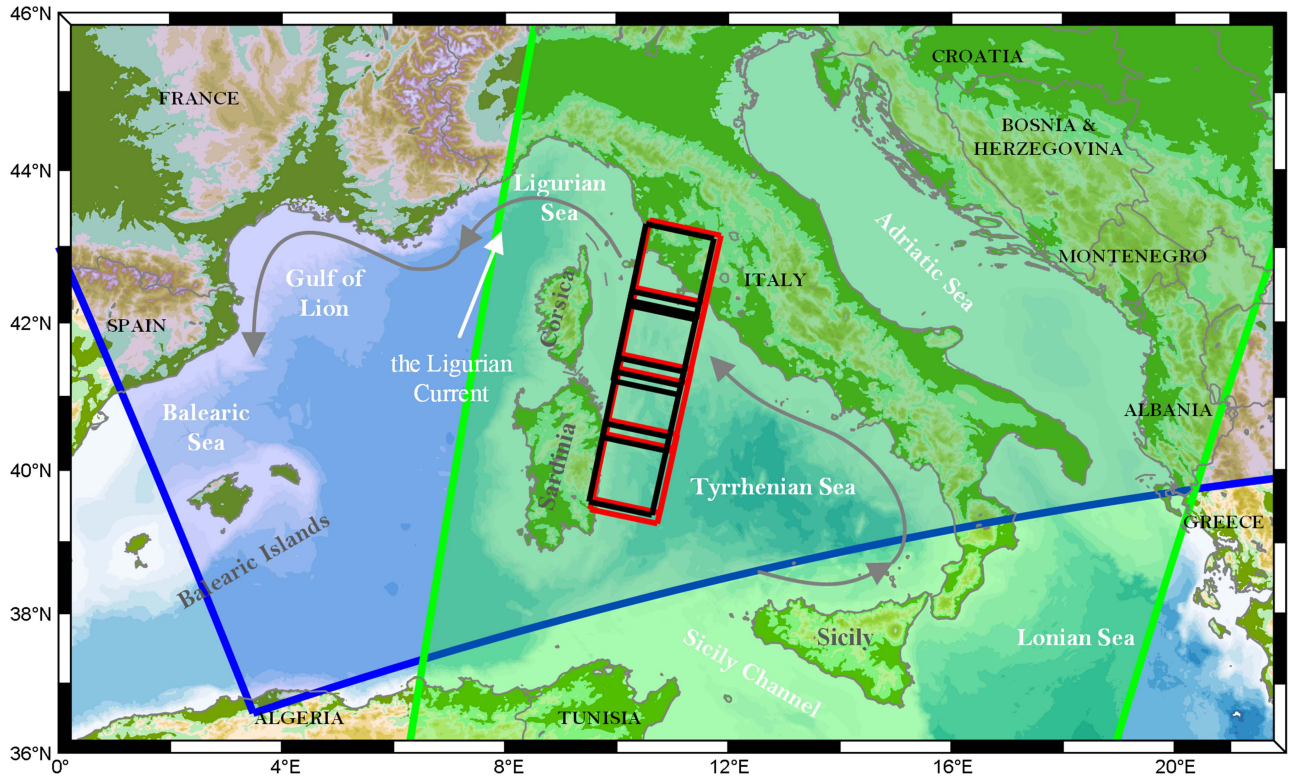

Fig. 1. Map of the study area in the northern Tyrrhenian Sea. The red, black, green, and blue areas are the coverage of envisat SAR, ERS-2 SAR, envisat MERIS, and aqua MODIS during the study period.

TABLE I
DETAILED INFORMATION OF SEQUENTIAL SAR AND OC IMAGES

Satellite	Sensor	Acquisition time (UTC)	Resolution	Swath (km)	Polarization/Common products
Envisat	SAR	20050321 09:33	30 m	100	VV
ERS-2	SAR	20050321 10:01	30 m	100	
Envisat	MERIS	20050321 09:33	1200m	1150	Chl\Kd490\Rrs443
Aqua	MODIS	20050321 12:00	1000m	2330	

selected as the search window S. The template window was moved within the search window in both the horizontal and vertical directions. Correlation coefficients were calculated for each movement. When the template window is moved by p and q in the horizontal and vertical directions, respectively, the correlation coefficient $r(p, q)$ is computed as follows:

$$r(p,q) = \frac{\operatorname{cov}\left[T\left(x_T, y_T\right), S'\left(x_T + p, y_T + q\right)\right]}{\sqrt{\operatorname{var}\left[T\left(x_T, y_T\right)\right] \operatorname{var}\left[S'\left(x_T + p, y_T + q\right)\right]}} \quad (1)$$

where S' denotes the area covered by the template when it moves within a search window.

After the template window has traversed the entire search window, the location with coordinates $(p_{\max}, q_{\max})$ that produces the MCC coefficient corresponds to the most likely displacement of ocean surface advection. The ocean surface current is obtained by dividing the displacement by the time interval Δt between the two images.

The current speed and direction at $P_0(x_T, y_T)$ can be calculated as follows:

$$v_{P_0} = \sqrt{\left(p_{\max}\Delta x\right)^2 + \left(q_{\max}\Delta y\right)^2} \Big/ \Delta t, \quad (2)$$

$$\theta_{P_0} = \tan^{-1}\left(\left(q_{\max}\Delta y\right)/\left(p_{\max}\Delta x\right)\right), \quad (3)$$

where, Δx and Δy in (2) and (3) are the pixel sizes in the x- and y- directions, respectively.

Finally, a grid of template windows was selected to provide a map of the advective surface velocity $\mathbf{V}$.

The size of the template window is important for current estimation. If the template is excessively large, the fine structure of the current field is lost. If the template size is excessively small, sufficient surface features cannot be obtained, leading to incorrect matching. Therefore, it is necessary to select an appropriate template window size. The MCC template size

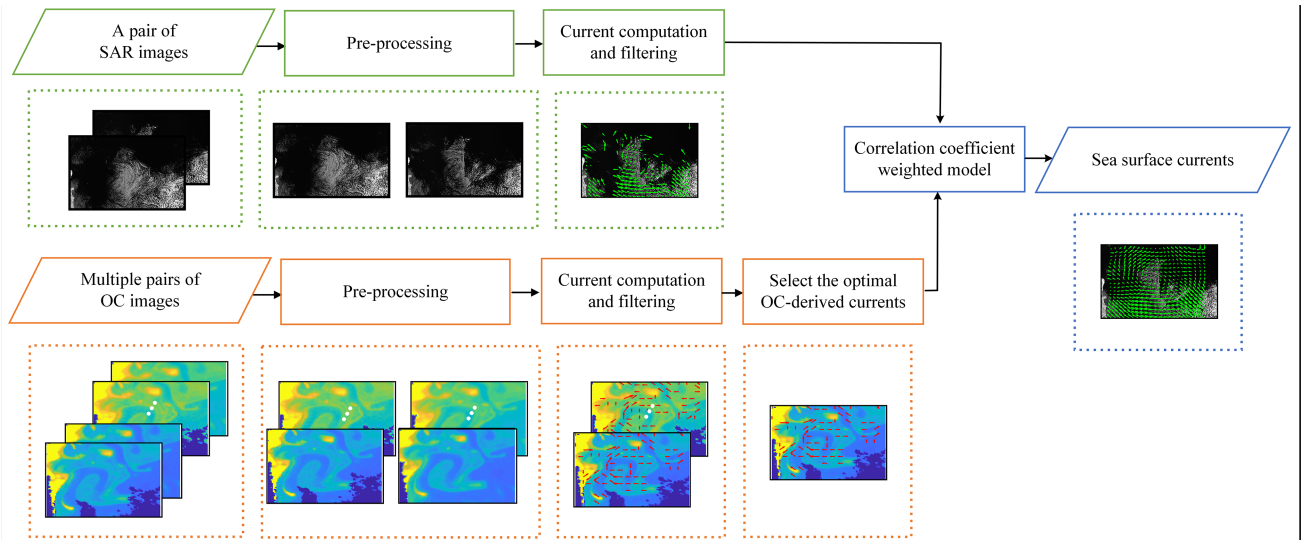

Fig. 2. Procedure of the proposed approach for SSC retrieval from sequential SAR and OC images.

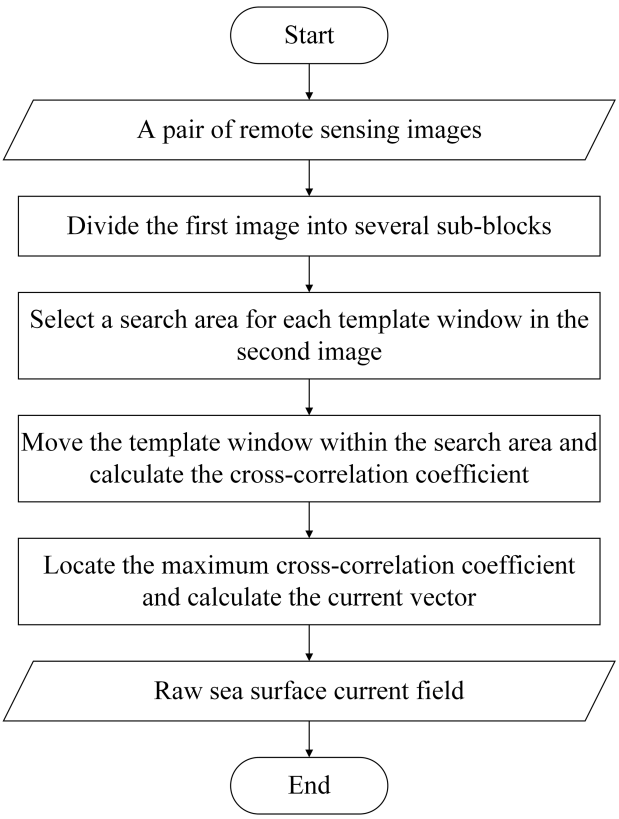

Fig. 3. Block diagram of MCC method for SSC retrieval.

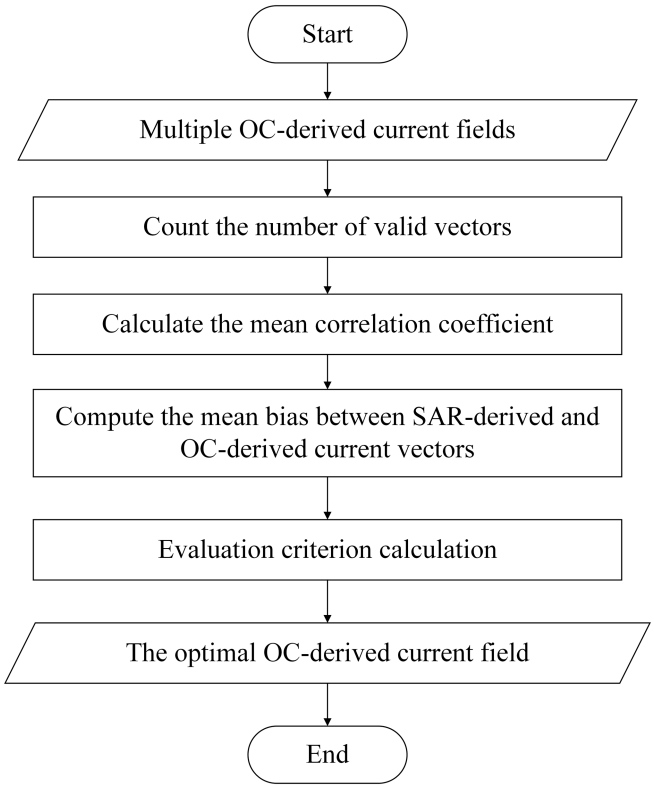

Fig. 4. Block diagram for selecting the optimal OC-derived currents.

estimation method described in a previous work [42] was used in this article to determine the template size.

B. Metrics for Evaluating OC-Derived Currents

Several OC products respond to different bio-optical and advective processes. The quality varies according to the currents derived from different OC products. Low-quality vectors involved in merging lead to poor merging results. Thus, the OC currents to be merged must be carefully selected from the Chl, Kd490, and Rrs443 derived currents. A block diagram for selecting the optimal OC-derived currents is shown in Fig. 4.

The following three parameters were used to evaluate the OC-derived currents: the mean correlation coefficient R_m, number of valid vectors N_v, and mean bias between the SAR and OC velocity values V_{bias}. The confidence of the current vectors

which is assessed using the correlation coefficient is the most important factor for current retrieval. Raw MCC currents were filtered using a correlation coefficient filter and a reciprocal filter. After filtering, the number of valid vectors N_v was counted to evaluate the production capacity of the valid velocity vectors. The mean correlation coefficient of the valid velocity vectors is calculated as follows:

$$R_m^k = \frac{1}{N_v^k} \sum_{i=1}^{M_1} \sum_{j=1}^{N_1} R_{i,j}^k, k = 1, 2, \ldots, K, \tag{4}$$

where R^k is the correlation coefficient matrix of size $M_1 \times N_1$ generated from the MCC calculation process of the kth OC product, $K = 3$.

The mean bias of valid velocity vectors between SAR-derived SSCs and the kth interpolated OC-derived SSCs with the size of $M_2 \times N_2$ is calculated as follows:

$$V_{\text{bias}}^k = \frac{1}{N_{\text{b}}^k} \sum_{i=1}^{M_2} \sum_{j=1}^{N_2} \left(\left| \mathbf{V}_{i,j}^{\text{SAR}} \right| - \left| \mathbf{V}_{i,j}^k \right| \right) \tag{5}$$

where N_{b}^k is the number of matching current pairs between the SAR-derived and the kth interpolated OC-derived current.

The evaluation criterion for the optimal OC-derived currents was defined by considering the mean correlation coefficient, number of valid vectors, and mean bias between the SAR and OC currents. The evaluation criterion F is calculated as follows:

$$F^k = 2 \left(\frac{R_m^k}{\sum_{k=1}^3 R_m^k} \right) + \left(\frac{N_v^k}{\sum_{k=1}^3 N_v^k} \right) - \left(\frac{V_{\text{bias}}^k}{\sum_{k=1}^3 V_{\text{bias}}^k} \right). \tag{6}$$

The currents derived from the different OC products were evaluated using criterion *F* and the current field. The highest value was selected as the optimal OC-derived current.

C. Calculation of Merged Currents and Eddy Kinematic Parameters

The image-derived SSC was mathematically a two-dimensional vector matrix. Every retrieved vector has its own correlation coefficient, representing the degree of confidence and a quantitative measure of how well the pattern matchup is correlated between two time-lapse patterns. Therefore, the correlation coefficient serves as the weight of the current vector. The SAR-derived and optimal-OC-derived currents were merged to obtain the complete current field. Based on the correlation coefficient weighted model [17], the merged current on pixels (i, j) is computed as follows:

$$\mathbf{V}_{i,j}^{\text{Merged}} = \frac{\mathbf{V}_{i,j}^{\text{SAR}} \cdot R_{i,j}^{\text{SAR}} + \mathbf{V}_{i,j}^{\text{OC}} \cdot R_{i,j}^{\text{OC}}}{R_{i,j}^{\text{SAR}} + R_{i,j}^{\text{OC}}} \tag{7}$$

where $\mathbf{V}_{i,j}^{\text{Merged}} (i = 1, 2, \ldots, M_2; j = 1, 2, \ldots, N_2)$ is the merged current vector for pixel (i, j); $\mathbf{V}_{i,j}^{\text{SAR}}$ and $\mathbf{V}_{i,j}^{\text{OC}}$ are vectors provided by the SAR-derived and interpolated OC-derived SSC, respectively, for pixel (i, j); $R_{i,j}^{\text{SAR}}$ and $R_{i,j}^{\text{OC}}$ are the correlation coefficients corresponding to the SAR-derived and OC-derived SSC.

Based on the geometric criteria of complete current fields, the eddy kinetic energy (EKE) is calculated from the velocity components using the following classical relation:

$$\text{EKE} = \frac{1}{2} \left(u_{\text{Merged}}^2 + v_{\text{Merged}}^2 \right) \tag{8}$$

where u_{Merged} and v_{Merged} denote the velocity components in the x- and y- directions, respectively.

To investigate the principal eddy characteristics of the study region, the vorticity ζ and divergence ψ are calculated as follows:

$$\zeta = \partial v_{\text{Merged}} / \partial x - \partial u_{\text{Merged}} / \partial y \tag{9}$$

$$\psi = \partial u_{\text{Merged}} / \partial x + \partial v_{\text{Merged}} / \partial y. \tag{10}$$

The shearing deformation rate S_{sh} and the stretching deformation rate S_{st} are calculated as follows:

$$S_{\text{sh}} = \partial v_{\text{Merged}} / \partial x + \partial u_{\text{Merged}} / \partial y \tag{11}$$

$$S_{\text{st}} = \partial u_{\text{Merged}} / \partial x - \partial v_{\text{Merged}} / \partial y. \tag{12}$$

IV. Results

This section outlines a case study that applies the proposed approach to derive SSCs in the Tyrrhenian Sea within the western Mediterranean. These derived SSCs were then compared with geostrophic currents obtained from altimetry. Utilizing the derived SSC field, eddy kinematic parameters were calculated to analyze the evolution characteristics of eddies.

A. Currents Derived From Sequential SAR Images

Envisat and ERS-2 SAR images were downloaded from the ESA. Radiation calibration was applied to all SAR images that were registered and mosaicked onto strips to obtain the complete study area. For faster processing, the SAR images were downsampled by a factor of 3 from a 12.5-m resolution to a 37.5-m resolution. Finally, the processed SAR images were used to estimate the currents using a template size of 101 × 101 pixels.

The raw velocity field output from the MCC method contained vectors at every grid point with varying correlation coefficient values. The correlation coefficient and reciprocal filters were used in the raw current fields to eliminate spurious vectors. First, a minimum correlation cutoff value was used to remove vectors resulting from low values of pattern cross-correlation. After filtering, most of the vectors with low reliability were removed; however, some rogue vectors remained. The reciprocal filter [43] allows a low correlation coefficient threshold to be set, thereby increasing the number of valid vectors obtained while also removing vectors that were obviously incorrect. After applying the reciprocal filter, several outlier vectors are successfully removed.

Fig. 5(c) shows the filtered current field derived from the sequential SAR images. The current field satisfied the principle of local consistency, and the results revealed many fine current structures. In particular, a clockwise (anticyclonic) eddy was observed in the lower part of the study area. However, the presence of extensive low backscatter areas in SAR images limits SSC retrieval because of the absence of traceable surfactant slicks.

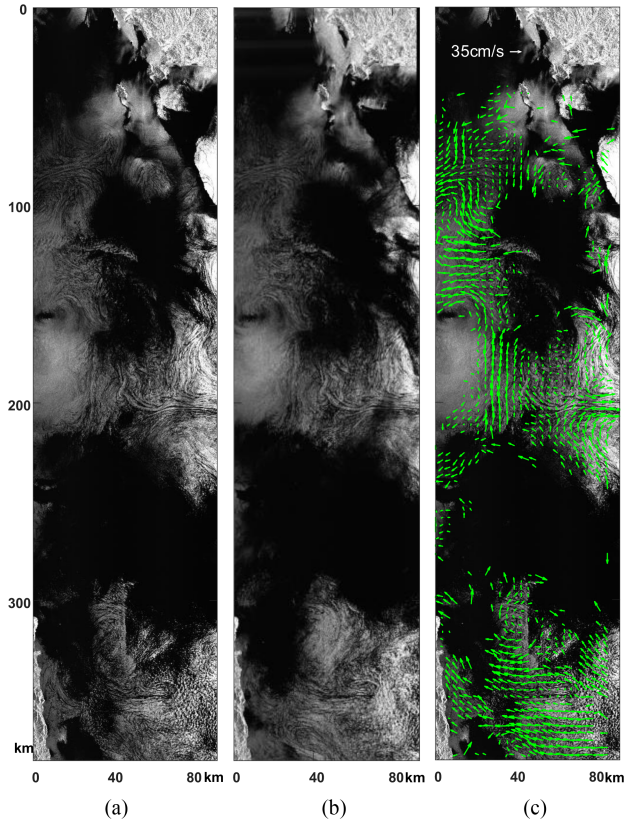

Fig. 5. Sequential SAR images and current field derived from the SAR images. (a) Envisat SAR image acquired at 09:33 UTC. (b) ERS SAR image acquired at 10:01 UTC on March 21, 2005. (c) Current field derived from the sequential SAR images (a) and (b).

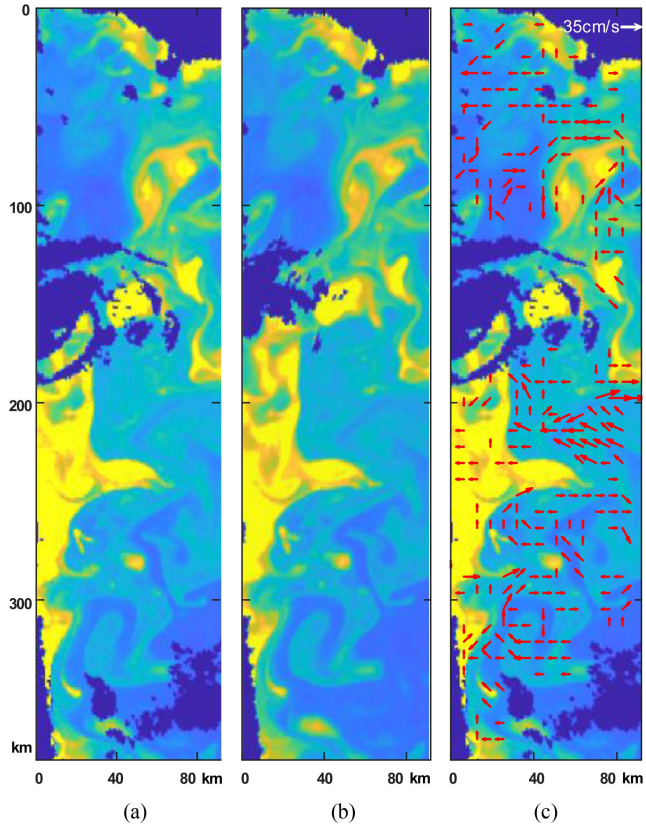

Fig. 6. Sequential Chl images and current field derived from the Chl images. (a) MERIS Chl image acquired at 09:33 UTC. (b) MODIS Chl image acquired at 10:01 UTC on March 21, 2005. (c) Derived current field.

The structure of the anticyclonic current field was incomplete. Other missing areas were identified in the study area.

B. Extraction and Evaluation of OC Derived Currents

1) Currents Derived From Different OC Products: Sequential OC images were acquired from MERIS and MODIS with spatial resolutions of 1200 and 1000 m, respectively. The same strip area as the SAR image was selected. The interval between the two strips was approximately 150 min. The OC products were resampled at the same pixel resolution. Sequential Chl, Kd490, and Rrs443 images are shown in Figs. 6, 7, and 8, respectively. Due to the failure of optical signals to penetrate clouds, most optical images suffer from data loss due to cloud cover, as shown in the dark blue areas between 100 and 200 km in Figs. 6 and 8. A comparison of panels (a) and (b) in Fig. 6, the dark blue area was reduced because of cloud movement during the acquisition of sequential images.

Current fields were derived from the registered sequential OC images with a template window size of 21×21 pixels. The correlation coefficient and reciprocal filters were used in the raw current fields to eliminate spurious vectors. The correlation coefficient filter threshold was 0.3. The MERIS and MODIS have three common products: Chl, Kd490, and Rrs443. Each product can be used independently to derive surface currents.

The current fields derived from the sequential Chl, Kd490, and Rrs443 images are illustrated in Figs. 6, 7, and 8, respectively. Two anticyclonic eddies can be observed at the bottom of the current field. Additionally, a dipole structure consisting of two coupled eddies appears at the top of the study area. As the two eddies were small, their fine current structures cannot be derived from the OC images, and only a cyclonic vortex surrounding the dipole can be observed in Figs. 6(c), 7(c), and 8(c). Compared with the current fields derived from Chl and Kd490, the currents derived from Rrs443 were poor because of the weak gradient features of the surface patterns in the sequential Rrs443 images.

All current fields derived from Chl, Kd490, and Rrs443 suffer from currents missing in the cloud covered areas, which are illustrated in the middle and lower parts of the study area. Compared with that of the SAR-derived currents shown in Fig. 5(c), the coverage of the OC-derived currents is evidently different. However, in overlapping areas, the SAR-derived and OC-derived currents have the same general circulation.

2) Evaluation of OC-Derived Currents: To evaluate the current fields derived from different OC products quantitatively, the distribution of the correlation coefficients and the number of valid current vectors were determined and are illustrated in Fig. 9. The mean correlation coefficient of the Chl-derived current field was 0.79, and the mean correlation coefficients of the Kd490 and Rrs443-derived current fields were 0.77 and 0.64, respectively. The current field derived from the Kd490 images

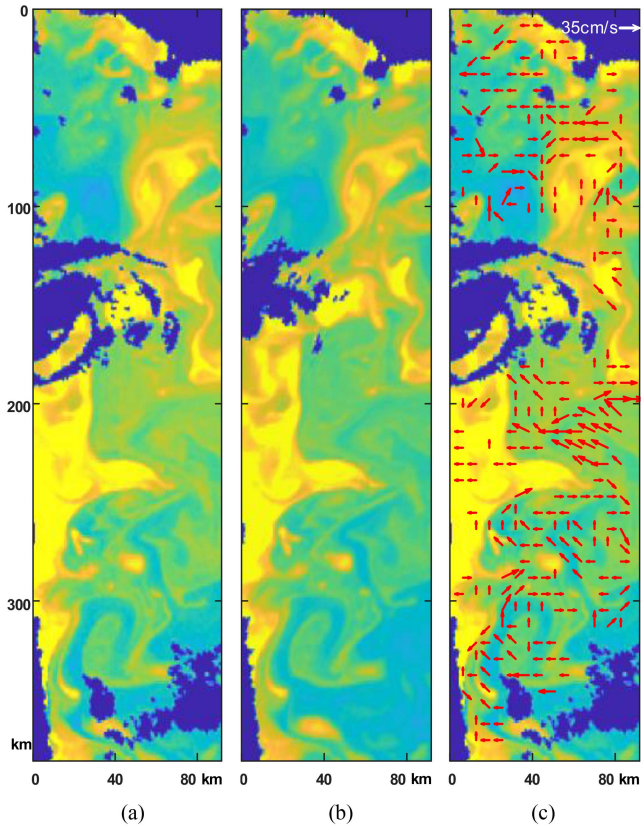

Fig. 7. Sequential Kd490 images and current field derived from Kd490 images. (a) MERIS Kd490 image acquired at 09:33 UTC. (b) MODIS Kd490 image acquired at 10:01 UTC on March 21, 2005. (c) Derived current field.

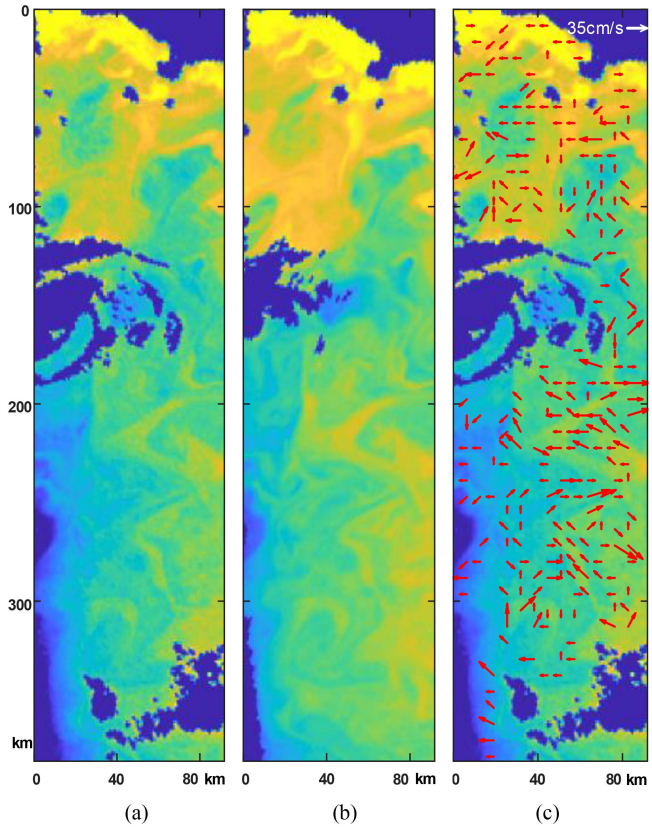

Fig. 8. Sequential Rrs443 images and current field derived from Rrs443 images. (a) MERIS Rrs443 image acquired at 09:33 UTC. (b) MODIS Rrs443 image acquired at 10:01 UTC on March 21, 2005. (c) Derived current field.

TABLE II
MEAN BIASES AND RMS ERRORS BETWEEN THE SAR-DERIVED AND OC-DERIVED CURRENTS IN MAGNITUDE AND DIRECTION

OC products	V_{bias} (cm/s)	θ_{bias} (deg)	V_{RMS} (cm/s)	θ_{RMS} (deg)
Chl	7.65	10.07	10.57	65.59
Kd490	7.56	13.22	10.62	73.67
Rrs443	6.01	5.61	10.28	69.70

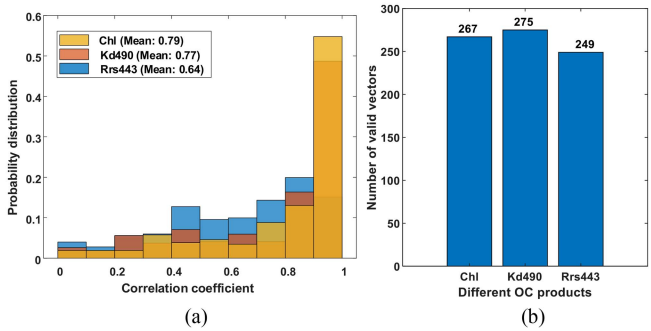

Fig. 9. Distribution of (a) correlation coefficients and (b) number of valid current vectors of Chl, Kd490, and Rrs443 derived current fields.

had the largest number of effective vectors of 275. For comparison with the SAR-derived currents, multiple OC-derived currents were interpolated to the same resolution. The mean biases between the SAR-derived and OC-derived currents, calculated using (5), are given in Table II. Owing to non-advective biological processes and different seawater penetration depths, the mean velocity biases of the OC-derived currents were slightly different. Further, the mean bias of the Chl-derived currents increased by 1.64 cm/s, compared with that of the Rrs443-derived currents.

Based on the mean correlation coefficient, the number of valid current vectors, and the mean bias between SAR and OC-derived currents, the criteria F calculated for Chl, Kd490, and Rrs443 derived currents using (6) were 0.70, 0.69, and 0.61, respectively. Therefore, the Chl-derived current field was selected as the optimal OC-derived currents to be merged.

C. Merging and Validation of the Currents

To maintain a fine current structure, the SAR-derived currents were unchanged, whereas the OC-derived currents and correlation coefficients were interpolated to the same spatial resolution as the SAR-derived SSCs. The SAR-derived and OC-derived SSCs were then merged according to (7). The merged SSCs have the same spatial resolution as the SAR-derived SSC. Owing to the local consistency of the SSCs, the missing velocity vectors

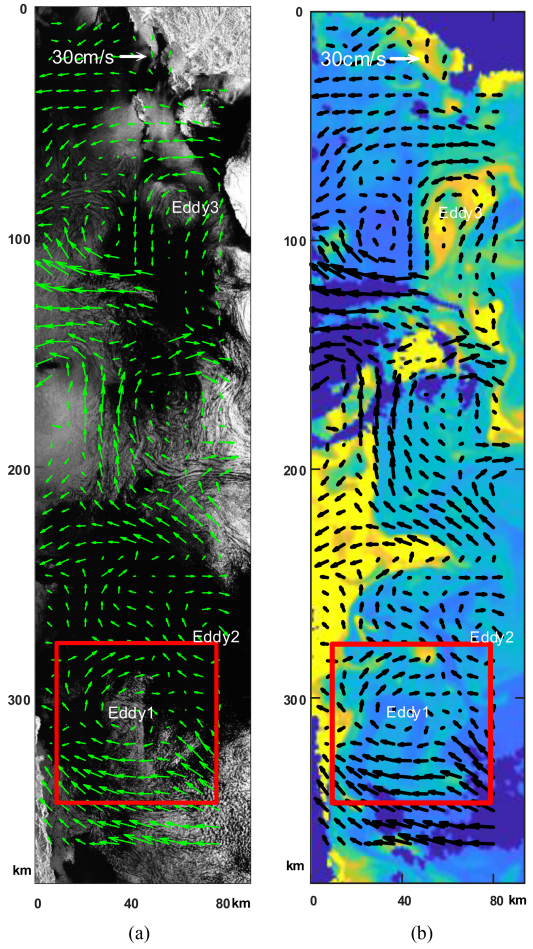

Fig. 10. Complete current field obtained by merging the SAR-derived currents and the Chl-derived currents superimposed on (a) envisat SAR image and (b) MERIS Chl image at 09:33 UTC on March 21, 2005. The red frame shows the area of interest selected as described in Section III-D.

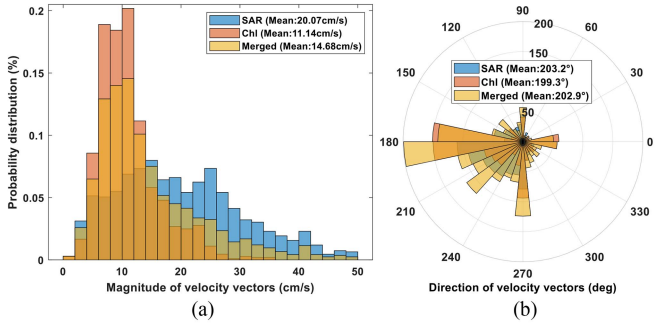

Fig. 11. Histograms of data distributions for the (a) magnitude and (b) direction of SAR-derived, Chl-derived, and merged currents.

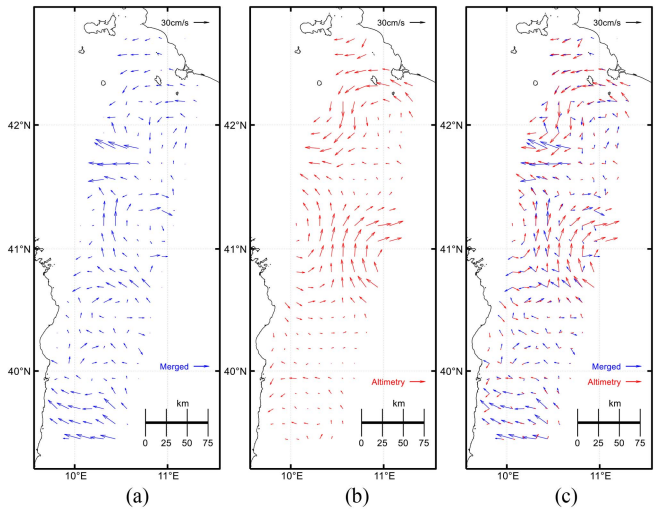

Fig. 12. Comparison of (a) merged and (b) geostrophic currents. (c) Current fields.

can be obtained by interpolation in nearby areas. The merged SSCs were then smoothed using mean filtering and downsampled by a factor of two for display purposes.

The merged current field is shown in Fig. 10. The missing current areas due to cloud cover in the Chl-derived current field were compensated by SAR-derived currents, as observed in the middle and lower parts of the study area. Moreover, the missing areas of the SAR-derived currents in the low backscatter areas were compensated by the Chl-derived currents to obtain a complete current field. The current structure of the anticyclonic eddy at the bottom of the study area was completed in a merged current field. Additionally, two other eddies (Eddies 2 and 3) were visible in the merged current field.

Statistical comparisons were performed for the SAR-derived, Chl-derived, and merged currents, as illustrated in Fig. 11. The mean velocities of the SAR-derived and Chl-derived currents were 20.07 and 11.14 cm/s, respectively, and the mean velocity of the merged currents was 14.68 cm/s. The mean velocity directions of the SAR-derived and Chl-derived currents were 203.2° and 199.3°, respectively, while that of the merged currents was 202.9°.

Satellite image-derived velocity observations using the MCC method produce total ocean currents (i.e., ageostrophic and geostrophic currents), which are likely wind-driven [10]. In this article, the wind speed was low, approximately 2–3 m/s, indicating a minimal impact on the image-derived currents. As there were no drifting buoy data for comparison, the accuracy of the merged currents was examined by comparing them with geostrophic currents from altimetry. The geostrophic currents were obtained from the Copernicus Marine Environment Monitoring Service (https://data.marine. Copernicus.eu/). We used the dataset "European Seas Gridded L4 Sea Surface Heights and Derived Variables Reprocessed 1993 Ongoing" (product identifier SEALEVEL_ EUR_PHY_L4_MY_008 _068). It consists of the daily mean geostrophic flow with a spatial resolution of 0.125°. The geostrophic currents were temporally interpolated to obtain the geostrophic flow at 12:00 UTC on March 21, 2005. For comparison, the merged currents were regridded to the same resolution as the geostrophic currents.

Fig. 12 shows a comparison between the merged current field and geostrophic current field. The same current structures were observed between the two current fields, particularly in the upper part of the study area. Both the merged and geostrophic currents capture the westward flow of the Ligurian Current [44],

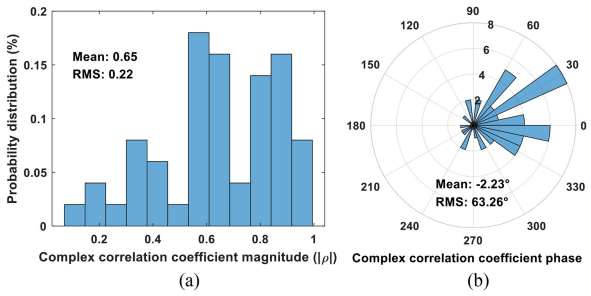

Fig. 13. Histograms of the complex correlation: (a) Magnitude and (b) phase difference between the regridded merged currents and geostrophic currents with a resolution of 0.5°.

indicating the correctness of the merged current in this article to a certain extent. However, because the merged currents presented the total ocean current [10], differences existed between the merged and verification currents.

A complex correlation was calculated to analyze the consistency of the merged currents with geostrophic currents quantitatively. The current vector is represented as a complex number V', defined by $V' = u + i \cdot v$, and V'^* is the complex conjugate. Therefore, the merged and geostrophic current vectors can be represented as V'_{Merged} and $V'_{\text{Altimeter}}$. The complex correlation between the merged and geostrophic current vectors is defined as follows [45]:

$$\rho = \frac{\langle V'_{\text{Merged}} \cdot V'_{\text{Altimeter}} \rangle}{\sqrt{\left[V'_{\text{Merged}} \cdot V'^*_{\text{Merged}}\right]\left[V'_{\text{Altimeter}} \cdot V'^*_{\text{Altimeter}}\right]}}. \quad (13)$$

The average magnitude correlation coefficient is defined as follows:

$$|\rho| = \sqrt{[\text{Re}(\rho)]^2 + [\text{Im}(\rho)]^2}. \quad (14)$$

The average angular phase difference is defined as follows:

$$\varphi = \tan^{-1}\left[\frac{\text{Im}(\rho)}{\text{Re}(\rho)}\right]. \quad (15)$$

The magnitude correlation is a measure of the relative magnitude variation between the merged and geostrophic current vectors. The phase angle gives the mean counterclockwise rotation of the merged current vectors with respect to the geostrophic current vectors and is only reasonable when the magnitude correlation is high [45]. Histograms of the complex magnitudes and phase differences between the merged and geostrophic currents with a resolution of 0.5° are shown in Fig. 13. The mean magnitude of the correlation coefficient was 0.65. The merged current field exhibited an average clockwise rotation of 2.23° relative to the geostrophic current field.

D. Oceanic Eddy Kinematics Analysis

There are several oceanic eddies in the study area. The anticyclonic eddy in the lower part was selected to calculate the oceanic eddy kinematic parameters using (8)–(12). Fig. 14(a) shows the scale of the eddy core boundaries with the corresponding maximum tangential velocities. A strong northwestern drift with

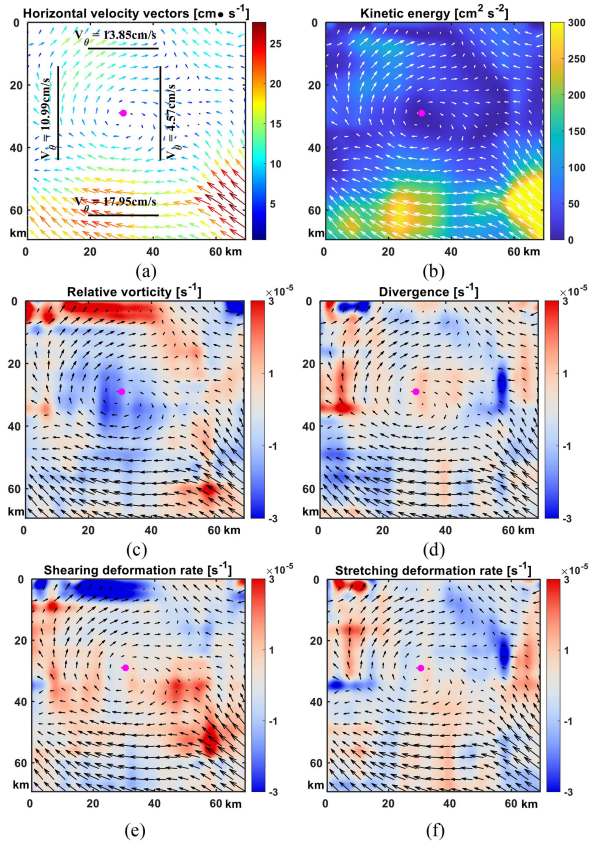

Fig. 14. Calculation results for the kinematic parameters for the magnified area over the anticyclonic eddy in the red frame of Fig. 10. (a) Scales of the eddy core boundaries with corresponding maximum tangential velocities. Maps of (b) kinetic energy, (c) relative vorticity, (d) horizontal divergence, and (e) shearing deformation rate, and (f) stretching deformation rate, calculated using (8)–(12). The red points represent the positions of the zero-velocity points.

an average velocity of 0.2–0.3 m/s can be observed in the lower right of the image, which may affect the eddy formation and restrain the scale of the eddy current structure. The resulting map, illustrated in Fig. 14(b), shows the levels of EKE varying from 200 to 300 cm^2s^{-2} at the bottom. The relative vorticity and horizontal divergence are shown in Fig. 14(c) and (d), respectively. The negative values of relative vorticity reveal the clockwise rotation of the eddy. The absolute values of the shearing and stretching deformation rates of 10^{-5}s^{-1} indicate that the anticyclonic eddy tended to deform and was not perfectly circular. Fig. 14(e) illustrates the high positive values of the shearing deformation rate at the lower right of the anticyclonic eddy, indicating compression in the northwest–southeast direction. The negative values of the stretching deformation rate at the upper right side indicate east–west compression, which explains the formed elliptical structure of the eddy with minor and major axes of approximately 30and 50 km, respectively.

V. Discussion

In this article, SSCs were derived using the MCC method with sequential SAR and OC images. The SAR-derived and OC-derived currents have the same general circulation but different spatial coverage. Merging SAR-derived and OC-derived

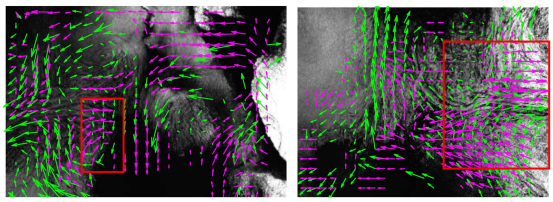

Fig. 15. Comparison between SAR-derived (green arrow) and interpolated Chl-derived (red arrow) currents before merging. (a) and (b) Overlapping areas selected for comparison.

currents overcomes the limitations of individual remote sensing instruments and provides a complete SSC field for eddy kinematic analysis.

The first issue that needs to be discussed is the difference in the SSCs derived from different remote-sensing images. Owing to the different resolutions of the SAR and OC images, the spatial resolutions of the SAR-derived and OC-derived SSCs were different. To maintain fine current structures, the SAR-derived currents were not changed, whereas the OC-derived currents and correlation coefficients were interpolated to the same spatial resolution as the SAR-derived SSCs, achieving the purpose of merging the currents.

Additionally, the MCC method extracts the average flow field during the acquisition of sequential images [10]. Owing to the constraints imposed by the satellite orbits, the acquisition times of the remote sensing image pairs from different sources were not the same, resulting in slight differences in the image-derived SSCs. In this article, the first images of the SAR and OC image pairs were acquired simultaneously, and the second image of the OC image pair was acquired with a 2-h lag compared to the second image of the SAR image pair. While there are discernible differences in certain areas between the SAR-derived and OC-derived SSCs, illustrated by the red boxes in Fig. 15(a) and (b), where the OC-derived current (red arrow) exhibits a slight positional offset relative to the SAR-derived current (green arrow), in most areas outside the red box, the SAR-derived and OC-derived SSCs demonstrated similar flow field structures. In the future, with the development of remote-sensing technology, the number of high-resolution remote-sensing images will gradually increase, and differences in the resolution and acquisition time of sequential images are expected to decrease.

Furthermore, polarimetric SAR images and hyperspectral images offer multi-polarization and multi-spectral information about oil slicks on the sea surface, showcasing significant potential in target detection and classification. Future research will focus on SSC retrieval using polarimetric SAR images, hyperspectral images, and other relevant remote sensing data, enhancing understanding of ocean dynamics and environmental monitoring capabilities.

VI. Conclusion

Sequential SAR and OC images were used for SSC retrieval and oceanic eddy kinematic analysis. We illustrate that the SAR-derived and OC-derived currents have the same general circulation, and demonstrate that the SAR and OC observations can supplement each other to obtain a complete current field. Different OC products were used to retrieve SSCs. The OC-derived currents were evaluated using the proposed evaluation criterion. Chl-derived currents were selected as the optimal OC-derived currents and compared with the Rrs443-derived and Kd490-derived currents. An approach is presented to merge SAR and Chl-derived currents to obtain a complete oceanic eddy current field. The merged current fields in the northern Tyrrhenian Sea agree well with the geostrophic currents obtained from altimetry, with a complex correlation coefficient of 0.65 in magnitude and 2.23° in phase. The merged current field was used to retrieve the kinematic parameters of an anticyclonic eddy, which successfully explained the elliptical structure of the eddy observed in OC images.

References

[1] J. J. M. Busecke and R. P. Abernathey, "Ocean mesoscale mixing linked to climate variability," *Sci. Adv.*, vol. 5, no. 1, Jan. 2019, Art. no. eaav5014.
[2] D. J. McGillicuddy Jr., "Mechanisms of physical-biological-biogeochemical interaction at the oceanic mesoscale," *Ann. Rev. Mar. Sci.*, vol. 8, pp. 125–159, Aug. 2016.
[3] D. Zhao, Y. Xu, X. Zhang, and C. Huang, "Global chlorophyll distribution induced by mesoscale eddies," *Remote Sens. Environ.*, vol. 254, Mar. 2021, Art. no. 112245.
[4] Y. Li, X. Li, J. Wang, and S. Peng, "Dynamical analysis of a satellite-observed anticyclonic eddy in the northern Bering Sea," *J. Geophys. Res., Oceans*, vol. 121, no. 5, pp. 3517–3531, Jun. 2016.
[5] M. Amani et al., "Remote sensing systems for ocean: A review (Part 1: Passive systems)," *IEEE J. Sel. Topics Appl. Earth Observ. Remote Sens.*, vol. 15, pp. 210–234, Dec. 2021.
[6] L. L. Fu and P.-Y. L. Traon, "Satellite altimetry and ocean dynamics," *Comptes Rendus Geosci.*, vol. 338, pp. 1063–1076, Jul. 2006.
[7] W. J. Emery, A. C. Thomas, M. J. Collins, W. R. Crawford, and D. L. Mackas, "An objective method for computing advective surface velocities from sequential infrared satellite images," *J. Geophys. Res.*, vol. 91, no. C11, pp. 12865–12878, Nov. 1986.
[8] S. R. Chubb, R. P. Mied, C. Y. Shen, W. Chen, T. E. Evans, and J. Kohut, "Ocean surface currents from AVHRR imagery: Comparison with land–based HF radar measurements," *IEEE Trans. Geosci. Remote Sens.*, vol. 46, no. 11, pp. 3647–3660, Nov. 2008.
[9] C. Heuzé, G. K. Carvajal, L. B. Eriksson, and M. Soja-Woźniak, "Sea surface currents estimated from spaceborne infrared images validated against reanalysis data and drifters in the Mediterranean Sea," *Remote Sens.*, vol. 9, no. 5, pp. 412–422, Apr. 2017.
[10] D. K. Matthews and W. J. Emery, "Velocity observations of the California current derived from satellite imagery," *J. Geophys. Res.*, vol. 114, no. C8, pp. 1–14, Aug. 2009.
[11] C. A. E. Garcia and L. S. Robinson, "Sea surface velocities in shallow seas extracted from sequential coastal zone color scanner satellite data," *J. Geophys. Res.*, vol. 94, no. C9, pp. 12681–12691, Sep. 1989.
[12] Z. Hu et al., "Characterizing surface circulation in the Taiwan strait during NE monsoon from geostationary ocean color imager," *Remote Sens. Environ.*, vol. 221, no. 1, pp. 687–694, Feb. 2019.
[13] R. I. Crocker, D. K. Matthews, W. J. Emery, and D. G. Baldwin, "Computing coastal ocean surface currents from infrared and ocean color satellite imagery," *IEEE Trans. Geosci. Remote Sens.*, vol. 45, no. 2, pp. 435–447, Feb. 2007.
[14] J. Liu, W. J. Emery, X. Wu, M. Li, C. Li, and L. Zhang, "Computing coastal ocean surface currents from MODIS and VIIRS satellite imagery," *Remote Sens.*, vol. 9, no. 10, Oct. 2017, Art. no. 1083.
[15] J. Liu, W. J. Emery, X. Wu, M. Li, C. Li, and L. Zhang, "Computing ocean surface currents from GOCI ocean color satellite imagery," *IEEE Trans. Geosci. Remote Sens.*, vol. 55, no. 12, pp. 7113–7125, Dec. 2017.
[16] Y. Shi, X. Zhou, X. Yang, L. Shi, and S. Ma, "Merging satellite ocean color data with Bayesian maximum entropy method," *IEEE J. Sel. Topics Appl. Earth Observ. Remote Sens.*, vol. 8, no. 7, pp. 3294–3304, Jul. 2015.

[17] H. Yang, R. Arnone, and J. Jolliff, "Estimating advective near-surface currents from ocean color satellite images," *Remote Sens. Environ.*, vol. 158, pp. 1–14, Mar. 2015.
[18] O. Shomina, O. Danilicheva, T. Tarasova, and I. Kapustin, "Manifestation of spiral structures under the action of upper ocean currents," *Remote Sens.*, vol. 14, no. 8, Apr. 2022, Art. no. 1871.
[19] M. D. King, S. Platnick, W. P. Menzel, S. A. Ackerman, and P. A. Hubanks, "Spatial and temporal distribution of clouds observed by MODIS onboard the Terra and Aqua satellites," *IEEE Trans. Geosci. Remote Sens.*, vol. 51, no. 7, pp. 3826–3852, Jul. 2013.
[20] A. Ciappa, L. Pietranera, A. Coletta, and X. Jiang, "Surface transport detected by pairs of COSMO-SkyMed ScanSAR images in the Qingdao region (Yellow Sea) during a macro–algal bloom in July 2008," *J. Mar. Syst.*, vol. 80, no. 1, pp. 135–142, Feb. 2010.
[21] Y. Ren, X.-M. Li, G. Gao, and T. E. Busche, "Derivation of sea surface tidal current from spaceborne SAR constellation data," *IEEE Trans. Geosci. Remote Sens.*, vol. 55, no. 6, pp. 3236–3247, Jun. 2017.
[22] I. E. Kozlov, E. V. Plotnikov, and G. E. Manucharyan, "Brief communication: Mesoscale and submesoscale dynamics in the marginal ice zone from sequential synthetic aperture radar observations," *Cryosphere*, vol. 14, no. 9, pp. 2941–2947, Sep. 2020.
[23] D. R. Lyzenga and G. O. Marmorino, "Measurement of surface currents using sequential synthetic aperture radar images of slick patterns near the edge of the Gulf Stream," *J. Geophys. Res., Oceans*, vol. 103, no. C9, pp. 18769–18777, Aug. 1998.
[24] W. A. Qazi, W. J. Emery, and B. Fox-Kemper, "Computing ocean surface currents over the coastal California current system using 30-min-lag sequential SAR images," *IEEE Trans. Geosci. Remote Sens.*, vol. 52, no. 12, pp. 7559–7580, Dec. 2014.
[25] A. K. Liu and M. K. Hsu, "Deriving ocean surface drift using multiple SAR sensors," *Remote Sens.*, vol. 1, no. 3, pp. 266–277, Jul. 2009.
[26] G. Akbarizadeh, "A new statistical-based kurtosis wavelet energy feature for texture recognition of SAR images," *IEEE Trans. Geosci. Remote Sens.*, vol. 50, no. 11, pp. 4358–4368, Nov. 2012.
[27] G. Akbarizadeh, G. A. Rezai-Rad, and S. B. Shokouhi, "A new region-based active contour model with skewness wavelet energy for segmentation of SAR images," *IEICE Trans. Inf. Syst.*, vol. E93-D, no. 7, pp. 1690–1699, Jul. 2010.
[28] F. Sharifzadeh, G. Akbarizadeh, and Y. Seifi Kavian, "Ship classification in SAR images using a new hybrid CNN–MLP classifier," *J. Indian Soc. Remote*, vol. 47, no. 4, pp. 551–562, Oct. 2018.
[29] F. Samadi, G. Akbarizadeh, and H. Kaabi, "Change detection in SAR images using deep belief network: A new training approach based on morphological images," *Inst. Eng. Technol. Image Process.*, vol. 13, no. 12, pp. 2255–2264, Apr. 2019.
[30] Z. Tirandaz, G. Akbarizadeh, and H. Kaabi, "PolSAR image segmentation based on feature extraction and data compression using weighted neighborhood filter bank and hidden Markov random field-expectation maximization," *Measurement*, vol. 153, Dec. 2020, Art. no. 107432.
[31] N. Aghaei, G. Akbarizadeh, and A. Kosarian, "Osdes_net: Oil spill detection based on efficient_shuffle network using synthetic aperture radar imagery," *Geocarto Int.*, vol. 37, no. 26, pp. 13539–13560, May 2022.
[32] N. Davari, G. Akbarizadeh, and E. Mashhour, "Corona detection and power equipment classification based on GoogleNet-AlexNet: An accurate and intelligent defect detection model based on deep learning for power distribution lines," *IEEE Trans. Power Del.*, vol. 37, no. 4, pp. 2766–2774, Aug. 2022.
[33] N. Aghaei, G. Akbarizadeh, and A. Kosarian, "GreyWolfLSM: An accurate oil spill detection method based on level set method from synthetic aperture radar imagery," *Eur. J. Remote Sens.*, vol. 55, no. 1, pp. 181–198, Feb. 2022.
[34] F. Mahmoudi Ghara, S. B. Shokouhi, and G. Akbarizadeh, "A new technique for segmentation of the oil spills from synthetic-aperture radar images using convolutional neural network," *IEEE J. Sel. Topics Appl. Earth Observ. Remote Sens.*, vol. 15, pp. 8834–8844, 2022.
[35] M. Bertacca, F. Berizzi, and E. D. Mese, "A FARIMA-based technique for oil slick and low-wind areas discrimination in sea SAR imagery," *IEEE Trans. Geosci. Remote Sens.*, vol. 43, no. 11, pp. 2484–2493, Nov. 2005.
[36] T.-S. Kim, K.-A. Park, X. Li, and S. Hong, "SAR-derived wind fields at the coastal region in the East/Japan Sea and relation to coastal upwelling," *Int. J. Remote Sens.*, vol. 35, no. 11/12, pp. 3947–3965, May 2014.
[37] L. Qi, M. Wang, C. Hu, and B. Holt, "On the capacity of Sentinel-1 synthetic aperture radar in detecting floating macroalgae and other floating matters," *Remote Sens. Environ.*, vol. 280, Aug. 2022, Art. no. 113188.
[38] V. Barale, "The European marginal and enclosed seas: An overview," in *Remote Sensing of the European Seas*, Berlin, Germany: Springer, 2008, pp. 3–22.
[39] C. Millot, "Circulation in the Western Mediterranean Sea," *J. Mar. Syst.*, vol. 20, no. 1–4, pp. 423–442, Apr. 1999.
[40] V. Fernández, D. E. Dietrich, R. L. Haney, and J. Tintoré, "Mesoscale, seasonal and interannual variability in the Mediterranean Sea using a numerical ocean model," *Prog. Oceanogr.*, vol. 66, no. 2–4, pp. 321–340, May 2005.
[41] M. Rast, J. L. Bezy, and S. Bruzzi, "The ESA medium resolution imaging spectrometer MERIS a review of the instrument and its mission," *Int. J. Remote Sens.*, vol. 20, no. 9, pp. 1681–1702, Nov. 2010.
[42] X. Yang, J. Chong, and L. Diao, "Estimating MCC template size for ocean surface currents extraction from sequential SAR images," in *Proc. Photon. Electromagn. Res. Symp.*, 2021, pp. 2859–2862.
[43] I. J. Barton, "Ocean currents from successive satellite images: The reciprocal filtering technique," *J. Atmos. Ocean. Technol.*, vol. 19, no. 10, pp. 1677–1689, Oct. 2002.
[44] M. H. Rio, P. M. Poulain, A. Pascual, E. Mauri, G. Larnicol, and R. Santoleri, "A mean dynamic topography of the Mediterranean sea computed from altimetric data, in-situ measurements and a general circulation model," *J. Mar. Syst.*, vol. 65, no. 1–4, pp. 484–508, Mar. 2007.
[45] P. K. Kundu, "Ekman veering observed near the ocean bottom," *J. Phys. Oceanogr.*, vol. 6, no. 2, pp. 238–242, Mar. 1976.

Xue Yang received the B.S. degree in electronic engineering from Dalian Maritime University, Dalian, China, in 2019. She is currently working toward the Ph.D. degree in signal and information processing with the Aerospace Information Research Institute, Chinese Academy of Sciences and the University of Chinese Academy of Sciences, Beijing, China.

Her research interests include microwave ocean remote sensing and image information processing.

Jinsong Chong (Senior Member, IEEE) received the B.S. degree from Jilin University, Changchun, China, in 1991, the M.S. degree from the Beijing University of Aeronautics and Astronautics, Beijing, China, in 2000, and the Ph.D. degree from the Graduate School, Chinese Academy of Sciences, Beijing, China, in 2003.

She was a Visiting Scholar with Monash University, Melbourne, VIC , Australia, in 2004. She was a Tan Chin Tuan Exchange Fellow with Nanyang Technological University, Singapore, in 2005. She is currently a Research Professor with the Aerospace Information Research Institute, Chinese Academy of Sciences. Her research interest focuses on microwave remote sensing of ocean.

Yawei Zhao received the B.S. degree from the China University of Mining and Technology, Xuzhou, China, in 2017, and the Ph.D. degree from the Aerospace Information Research Institute, Chinese Academy of Sciences and the University of Chinese Academy of Sciences, Beijing, China, in 2022.

He is currently with the Aerospace Information Research Institute, Chinese Academy of Sciences. His research interests include radar signal processing and microwave remote sensing of ocean.